# Supplementary information

## Bio-inspired Carbon Cathodes with Sub-Nanometer Confinement for High-Performance Zinc-Ion Storage

Xiaohan Jin[a], Yaru Li[a], Nannan Chen[b], Ying Yang[a], Kunyu Xu[a], Jinzhuang Guo[a], Liming Dong[a], Jun Li*[c], He Liu[a] and Aijun Guo*[a]

[a] State Key Laboratory of Heavy Oil Processing, College of Chemistry and Chemical Engineering, China University of Petroleum (East China), Qingdao, 266580, China.

[b] School of Materials Science and Engineering, China University of Petroleum, Qingdao 266580 China.

[c] School of Chemical Engineering and Technology, North University of China, Taiyuan 030051, China.

*[a] Corresponding author: Aijun Guo

*E-mail: ajguo@upc.edu.cn.*

*[b] Corresponding author: Jun Li

*E-mail: lijun2015@nuc.edu.cn.*

## Experimental sections

### *Materials and reagents:*

Both isotropic coke (ISC) and anisotropic coke (ANC) samples were synthesized in the laboratory setting. Zinc sulfate heptahydrate ($ZnSO_4 \cdot 7H_2O$, AR), potassium hydroxide (KOH, AR), sodium bicarbonate ($NaHCO_3$), sodium carbonate ($Na_2CO_3$), sodium hydroxide (NaOH) and N-Methylpyrrolidone (NMP, AR) were procured from Shanghai Macklin Biochemical Technology Co., Ltd. Conductive acetylene black and polyvinylidene fluoride (PVDF) were acquired from Canrd. Zinc foils (99.99%) and titanium foils (99%) with thicknesses of 0.05 mm and 0.02 mm were sourced from Hefei Wenghe Metal Materials Co., Ltd. CR2032. Glass microfiber separators (GF/D) were obtained from Whatman. The in-situ battery cell was supplied by Shenzhen Fana Technology Co., China. The gel electrolytes were purchased from Shanghai Yanwen Technology Co., Ltd. Deionized water was utilized in the preparation of the aqueous electrolyte.

### *Preparation of porous carbon materials:*

In the preparation of the samples, 0.5 g of ISC was precisely weighed using an analytical balance. The ISC was then mixed with KOH at mass ratios of 1:1, 1:2, and 1:3, respectively. The resulting mixtures were transferred to nickel crucibles and positioned at the center of a tube furnace. The furnace was heated to 800°C at a rate of 5°C $min^{-1}$ under a nitrogen atmosphere and maintained at this temperature for 2 h. After the activation process, the furnace was allowed to cool down naturally to room temperature. Following the alkali activation process, the porous carbon materials were washed with 1M HCl to neutralize residual alkali and subsequently rinsed repeatedly with deionized water until the filtrate reached a neutral pH. The final products, labeled as ISC-1, ISC-2, and ISC-3, were obtained based on the mass ratios of KOH to ISC used in the preparation.

For comparison, ANC was used as an alternative precursor following the same procedure. Specifically, 0.5 g of ANC was mixed with KOH at identical mass ratios (1:1, 1:2, and 1:3), transferred to nickel crucibles, and subjected to the same heat treatment under identical conditions. The resulting samples were labeled as ANC-1, ANC-2, and ANC-3, corresponding to the respective mass proportions of KOH to ANC.

The activation mechanism of KOH is as follows [1]:

$$KOH + C \rightarrow K_2CO_3 + K_2O + H_2 \quad (1)$$

$$K_2CO_3 \rightarrow CO_2 + K_2O \quad (2)$$

$$K_2CO_3 + C \rightarrow CO + K \quad (3)$$

$$CO_2 + C \rightarrow CO \quad (4)$$

$$K_2O + C \rightarrow CO + K \quad (5)$$

***Materials characterization:***

The morphology and microstructure of all samples were examined using a field emission scanning electron microscope (SEM, JSM-7500 Prime) and a high-resolution transmission electron microscope (TEM, FEI Talos F200X). The crystalline structures were characterized by X-ray diffraction (XRD) using a PANalytical X'Pert$^3$ diffractometer with Cu Kα radiation (λ = 1.5418 Å) at a scan rate of 5°/min. X-ray photoelectron spectroscopy (XPS) was conducted on an Escalab 250Xi system (Thermo Fisher Scientific) to analyze the surface chemical composition. The specific surface area (SSA) and pore size distribution of the carbon materials were determined by nitrogen gas adsorption analysis at 77.3 K using a Quantum chromatograph. Dynamic contact angle measurements were carried out on an SZ10-JC2000C instrument. Optical images were obtained using a metallographic microscope (XP4, Shanghai Milite Precise Instrument Co., Ltd.) equipped with a custom-built in situ optical electrochemical cell. Raman spectra were recorded on a Horiba LabRAM HR Evolution system using a He/Ne laser (λ = 532 nm, power = 4.9 mW). The specimens for structural characterization were prepared using standard procedures. For SEM imaging, the powder was directly affixed to an aluminum stub using conductive carbon tape without subsequent coating. For TEM analysis, the powder was dispersed in ethanol via 30 min ultrasonication, followed by the deposition of a droplet of the suspension onto a lacey carbon-coated copper grid and drying at ambient temperature. Meanwhile, for XPS measurements, the powder was pressed into a pellet and analyzed without any prior surface treatment to prevent potential contamination.

***Electrochemical measurements:***

To fabricate the cathode, ISC or ANC powders, acetylene black, and polyvinylidene difluoride (PVDF) were mixed in a mass ratio of 8:1:1 in 500 μL NMP solution for 6 h. The resulting slurry was uniformly coated on a titanium current collector with a thickness of 120 μm using a coating device and dried in a vacuum drying oven at 80℃ for 12 h. The resulting film was then pressed under 50 psi to ensure good adhesion and electrical contact. The active loading mass was about 0.8 mg cm$^{-2}$. The button batteries were assembled in the order of porous carbon cathode, electrolyte film, Zn anode, gasket, and shrapnel. All batteries were allowed to rest for 12 h before testing. Cyclic voltammetry (CV) and electrochemical impedance spectroscopy (EIS) were carried out using a DH7000D electrochemical workstation (Jiangsu Donghua Testing Technology Co., Ltd.). Galvanostatic charge-discharge (GCD) tests and constant current cycling were conducted with a CT2100A potentiostat (Wuhan LAND Electronics, China). All electrochemical measurements, including cycling performance, were

conducted at 30℃.

To reveal the energy storage kinetics of the electrode materials, this paper decouples the capacitance-controlled and diffusion-controlled processes using Dunn's method. [2] This method is based on the CV curves of the electrode materials at different sweep rates.

$$i(v) = a \times v^{b}$$

$$\log i(v) = \log a + b \log v$$

$$i(v) = k_1 \times k_2 v^{-0.5}$$

In the above equations, $i$ (A) represents the anodic current at different scan rates at a specific voltage, and $v$ ($V \cdot s^{-1}$) is the scan rate. The parameters a, b, $k_1$, and $k_2$ are constants, where $k_1 v$ corresponds to the capacitance-controlled process, and $k_2 v^{-0.5}$ corresponds to the diffusion-controlled process.

The ion diffusion coefficient ($D$) is a physical parameter that reflects the rate at which electrolyte ions diffuse within the electrode material and can be calculated from the electrochemical impedance spectroscopy (EIS) data using the following equation [3]:

$$Z' = \sigma \omega^{-0.5} + R_s + R_{ct}$$

$$D = \frac{R^2 T^2}{2A^2 C^2 n^4 F^4 \sigma^2}$$

In this equation, $Z'$ and $\omega$ represent the real part of the impedance and the corresponding angular frequency in the low-frequency region, respectively. R, T, A, n, F, C, and $\sigma$ denote the gas constant, temperature, effective electrode area, number of electrons transferred, Faraday constant, ion concentration, and Warburg factor, respectively.

According to the GCD curve, the specific capacity ($C_m$, mAh $g^{-1}$) of the ZIHC was calculated using the following equation [4]:

$$C_m = \frac{I \times \Delta t}{3.6 \times m}$$

where $I$ (A) is the discharge current, $\Delta t$ (s) is the discharge time, and $m$ (g) is the mass of the active material.

The energy density ($E_m$, Wh $kg^{-1}$) of a zinc-ion capacitor is calculated using the following equation [5]:

$$E_m = \frac{C_m \times \Delta V^2}{7.2}$$

In this equation, $C_m$ (F $g^{-1}$) and $\Delta V$ (V) represent the specific capacitance and voltage window of the zinc-ion capacitor, respectively.

The power density ($P_m$, W $kg^{-1}$) for both supercapacitors and zinc-ion capacitors is calculated as:

$$P_m = \frac{P_m \times 3600}{\Delta t}$$

Here, $E_m$ (Wh $kg^{-1}$) and $\Delta t$ (s) represent the energy density and the discharge time obtained from the GCD curve, respectively.

**DFT calculations**

In this work, density functional theory (DFT) calculations were conducted using the Cambridge Serial Total Energy Package (CASTEP) code. [6] The generalized gradient approximation (GGA), as formulated by Perdew-Burke-Ernzerhof (PBE), was utilized to address electronic exchange-correlation interactions. A plane-wave basis set cutoff energy of 400 eV was employed. For the optimization of geometry and lattice parameters, Brillouin zone integration was performed using a 4×4×1 k-point sampling. The equilibrium geometry and lattice constants were refined with a total energy convergence threshold of $10^{-5}$ eV, maintaining a maximum atomic stress of 0.01 eV/Å and a maximum overall stress of 0.5 GPa. Density mixing electronic minimization was implemented, and the self-consistent field (SCF) tolerance was set to "fine," ensuring high accuracy with an energy convergence criterion of $10^{-6}$ eV per atom. The interaction energy ($E_{int}$) is determined using the equations:

$$E(\text{int}_1)=E(\text{total}_1)-E(Zn^{2+})-E(\text{graphene}) \quad (1)$$

$$E(\text{int}_2)=E(\text{total}_2)-E(Zn(H_2O)_6^{2+})-E(\text{graphene}) \quad (2)$$

in which $E(\text{total}_1)$, $E(\text{total}_2)$, $E(Zn^{2+})$, $E(Zn(H_2O)_6^{2+})$ and E(graphene) represent the energies of $Zn^{2+}$ adsorbed on double layer graphene, $Zn(H_2O)_6^{2+}$ adsorbed on double layer graphene, the $Zn^{2+}$, the $Zn(H_2O)_6^{2+}$ molecule and the double-layer graphene, respectively.

**DRT analysis**

Distribution relaxation times (DRT) from the EIS data were calculated using Matlab R2023b with the DRT-TOOLS toolbox, developed by the research group of Professor Francesco Ciucci. DRT TOOLS is freely available at the following site: https://github.com/ciuccislab.

**Quantification of Acidic Surface Functional Groups by Boehm Titration**

The concentration of acidic oxygen functional groups on carbon materials was quantitatively determined using the classical Boehm titration method. [7, 8] In a standard procedure, approximately 0.1 g of each carbon sample was accurately weighed and separately introduced into 25 mL of 0.1 M aqueous solutions of $NaHCO_3$, $Na_2CO_3$, and NaOH. The mixtures were sealed and agitated for 24 h at room temperature to ensure adsorption equilibrium

between the solid surfaces and the alkaline solutions. After equilibration, the suspensions were filtered to remove the carbon particles. A 10 mL aliquot of each filtrate was then precisely extracted and subjected to back-titration using a standardized 0.1 M HCl solution. The concentrations of the acidic functional groups were calculated based on the volume of HCl consumed, applying the following established principles:

i) The concentration of carboxyl groups was derived from the HCl consumed by the $NaHCO_3$ supernatant, which selectively neutralizes the strongest acidic sites.

ii) The concentration of laconic groups was calculated from the difference in HCl consumption between the $Na_2CO_3$ titration (to a methyl orange endpoint) and the $NaHCO_3$ titration.

iii) The concentration of phenolic hydroxyl groups was determined from the difference in HCl consumption between the NaOH titration and the $Na_2CO_3$ titration (to a phenolphthalein endpoint).

All experiments were conducted in duplicate to ensure reproducibility, and the average values are reported.

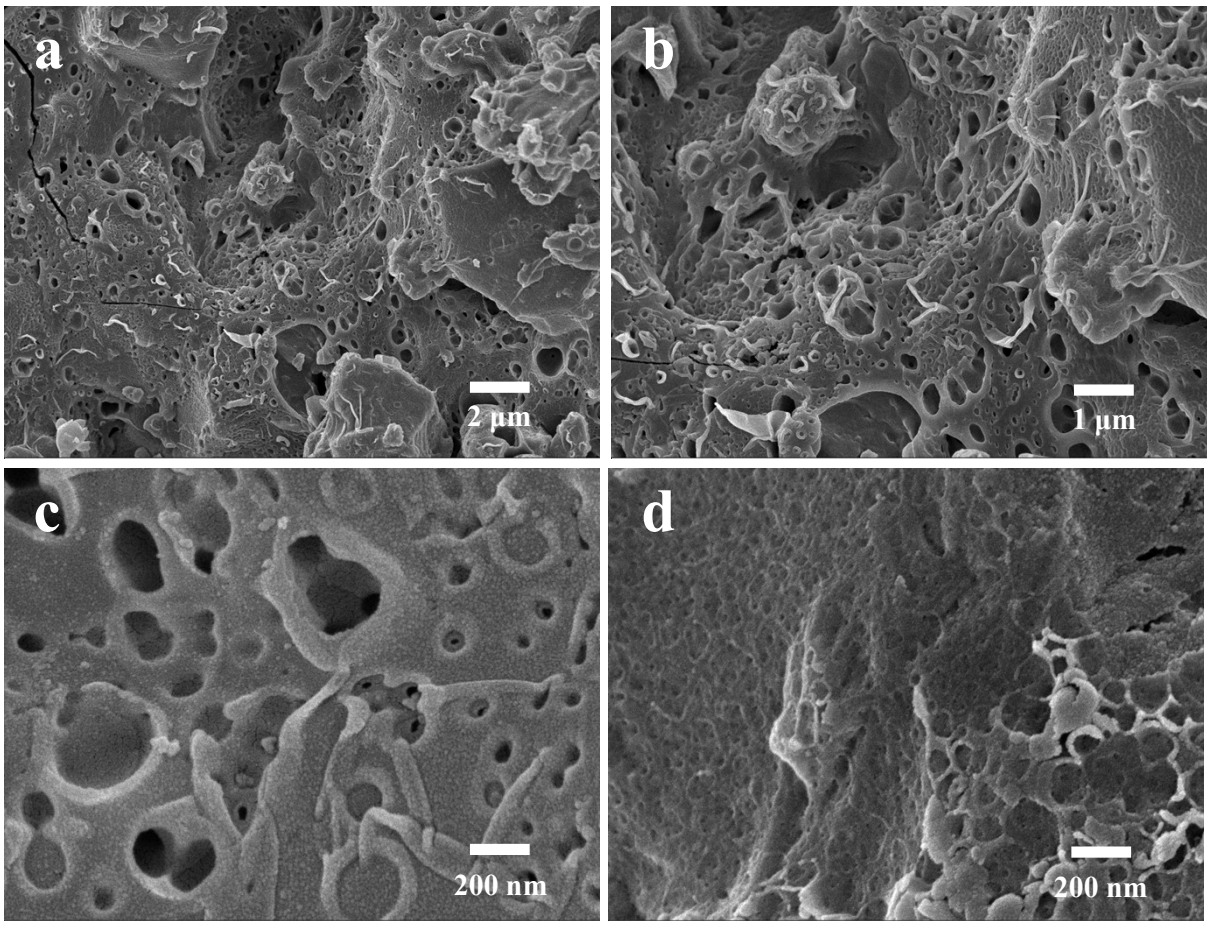


**Fig. S1 a-d.** SEM Images of ISC-2 at different resolutions

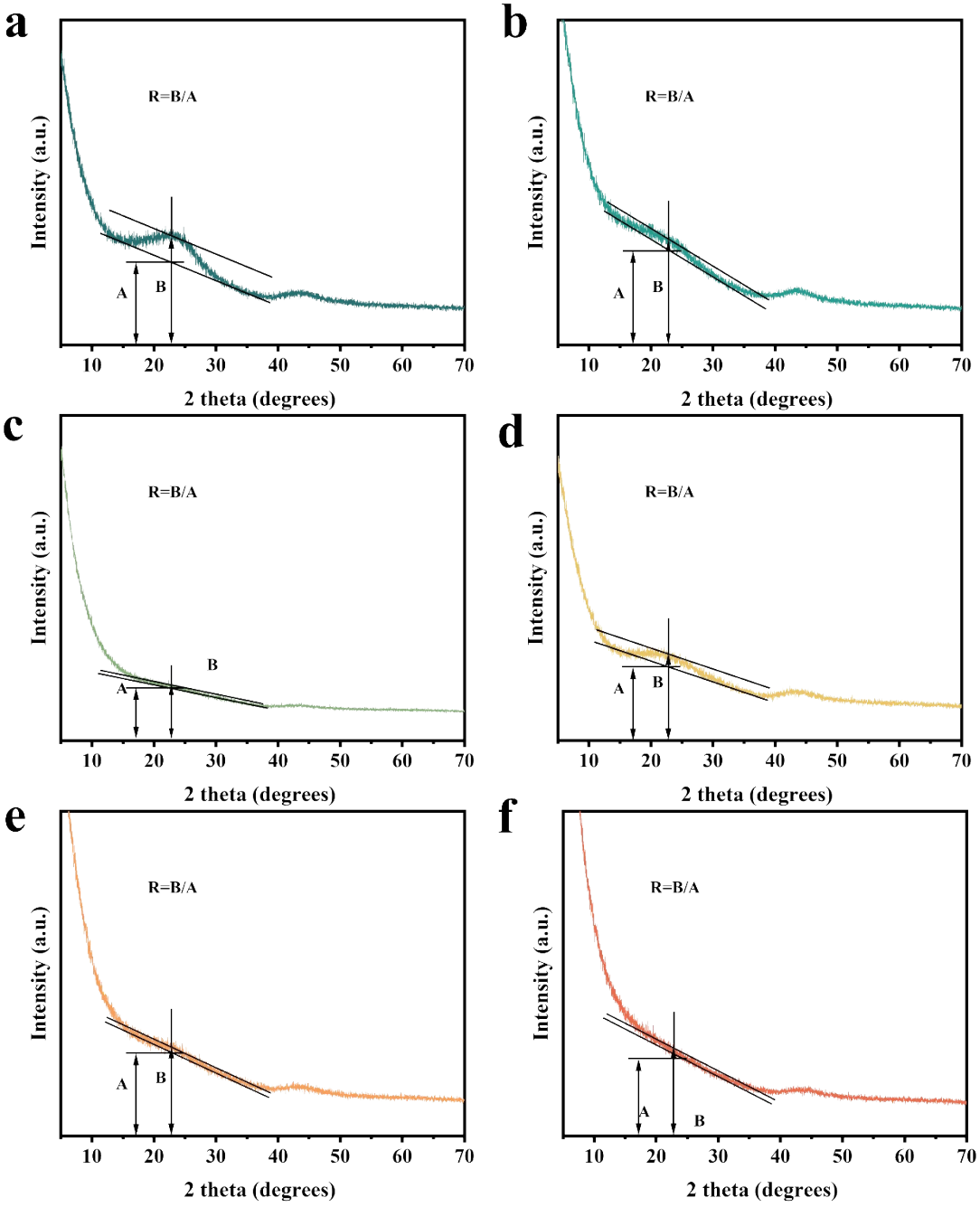


**Fig. S2.** The methodology for calculating R-values in: a) ANC-1, b) ANC-2, c) ANC-3, d) ISC-1, e) ISC-2 and f) ISC-3.

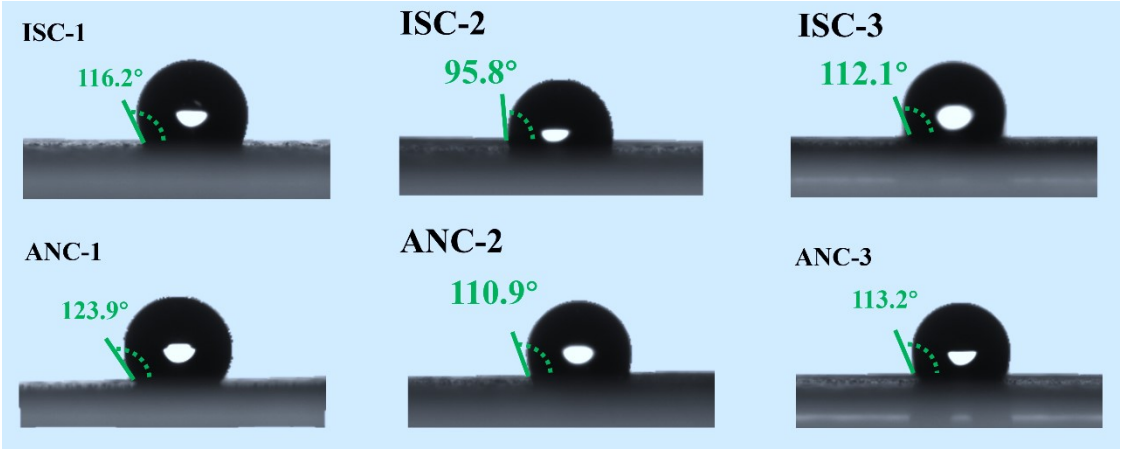


**Fig. S3.** Contact angles of ANC-1, ANC-2, ANC-3, ISC-1, ISC-2 and ISC-3.

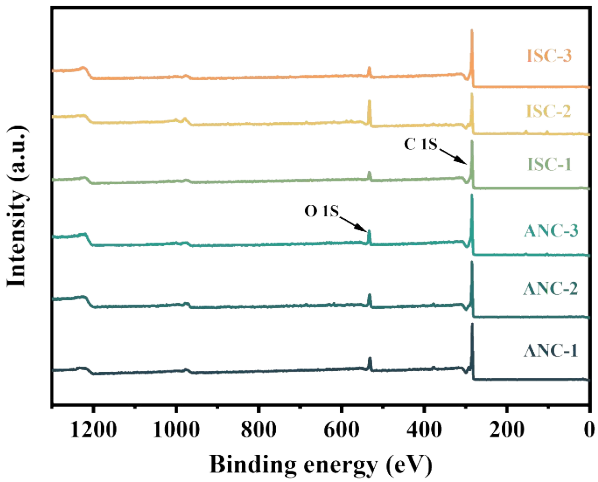


**Fig. S4.** The XPS spectrum of ANC-1, ANC-2, ANC-3, ISC-1, ISC-2 and ISC-3.

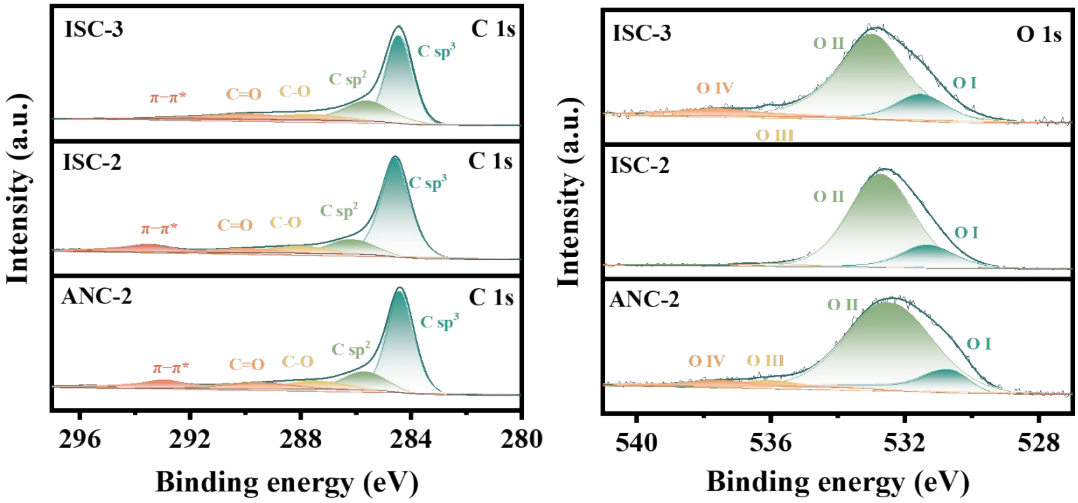


**Fig. S5.** The XPS spectrum of ANC-1, ANC-2, ANC-3, ISC-1, ISC-2 and ISC-3.

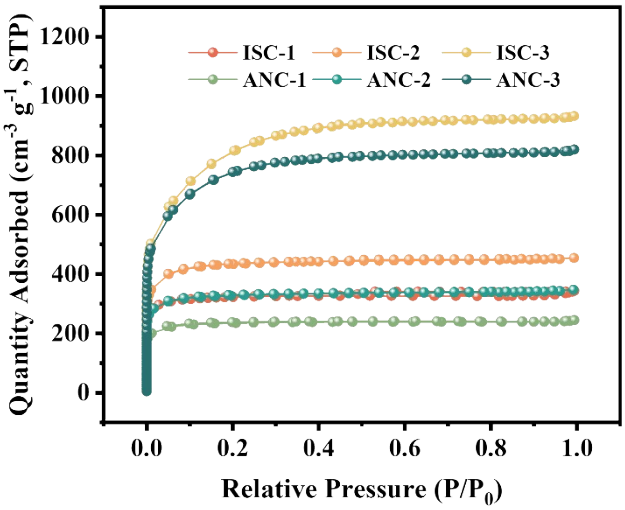


**Fig. S6.** $N_2$ adsorption-desorption isotherms of ANC-1, ANC-2, ANC-3, ISC-1, ISC-2 and ISC-3.

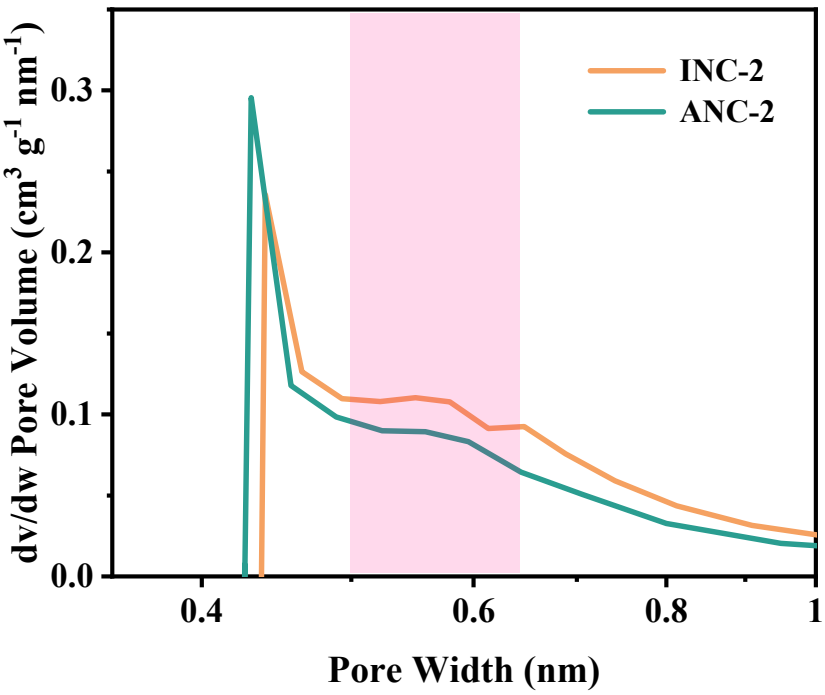


**Fig. S7.** The pore size distribution for ANC-2 and ISC-2 is based on the HK model.

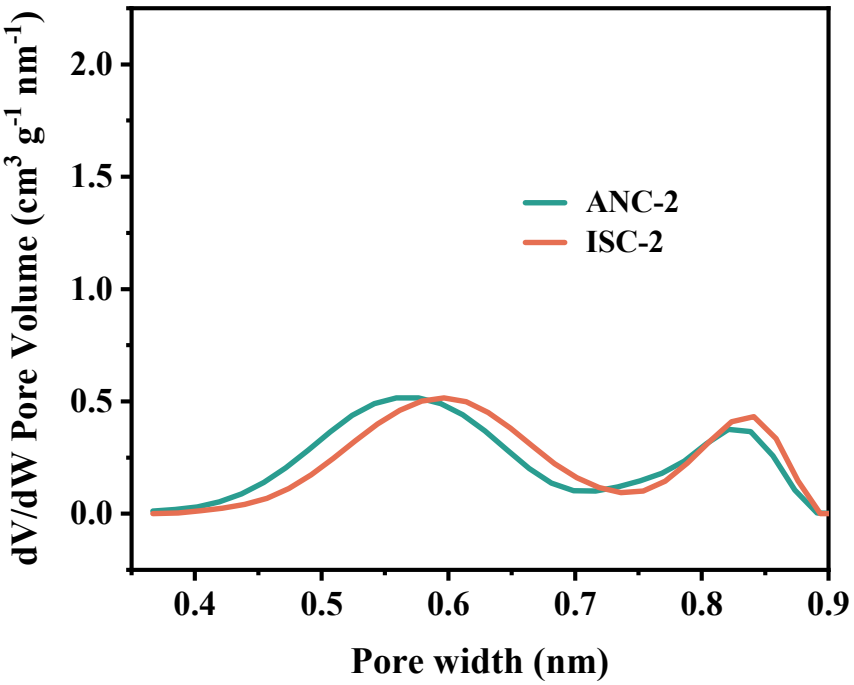


**Fig. S8.** $CO_2$ adsorption-derived pore size distributions for ISC-2 and ANC-2 samples.

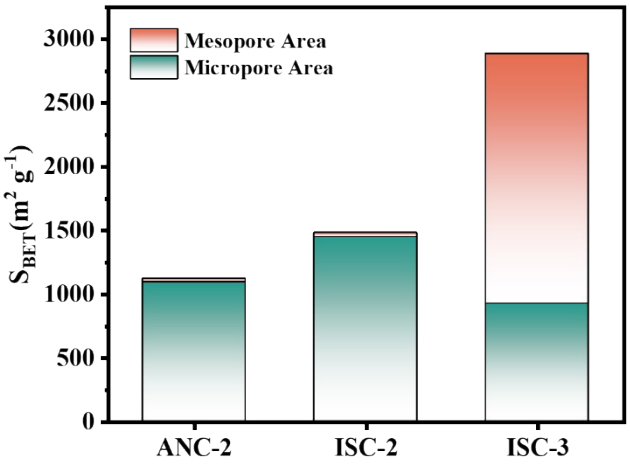


**Fig. S9.** Specific surface area distributions of ANC-2, ISC-2 and ISC-3.

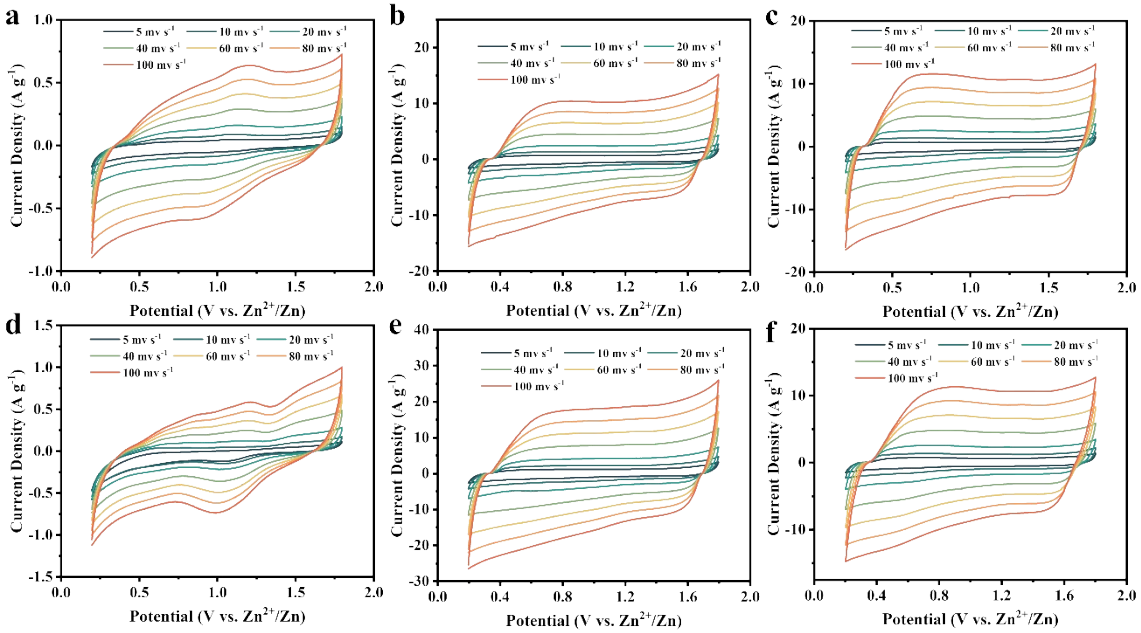


**Fig. S10.** CV curves of a) ANC-1, b) ANC-2, c) ANC-3, d) ISC-1, e) ISC-2 and f) ISC-3 from 5 to 100 mV $s^{-1}$.

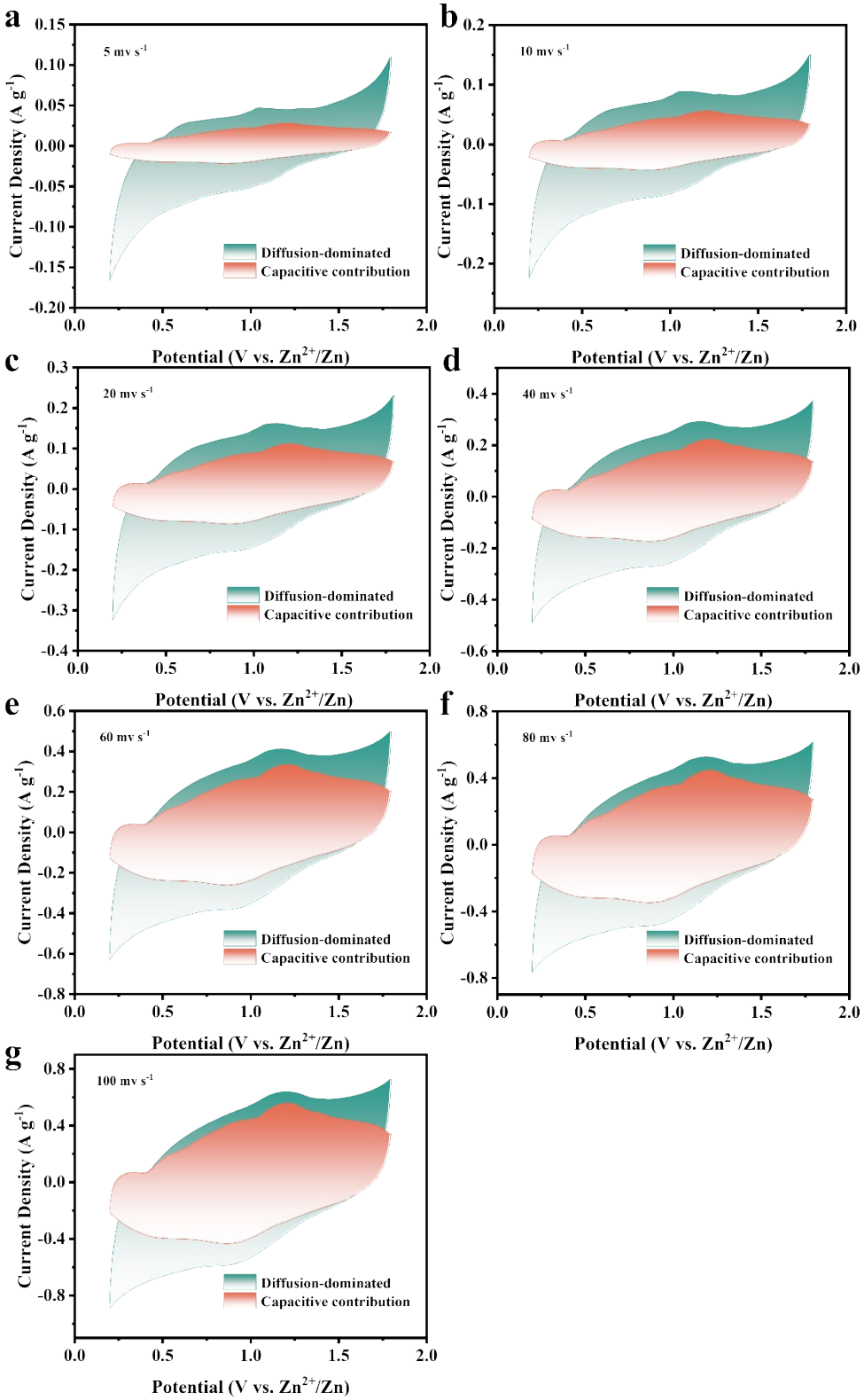


**Fig. S11.** (a - g) Capacitive-controlled and diffusion-dominated contributions of ANC-1 based AZICs from 5 to 100 mV $s^{-1}$

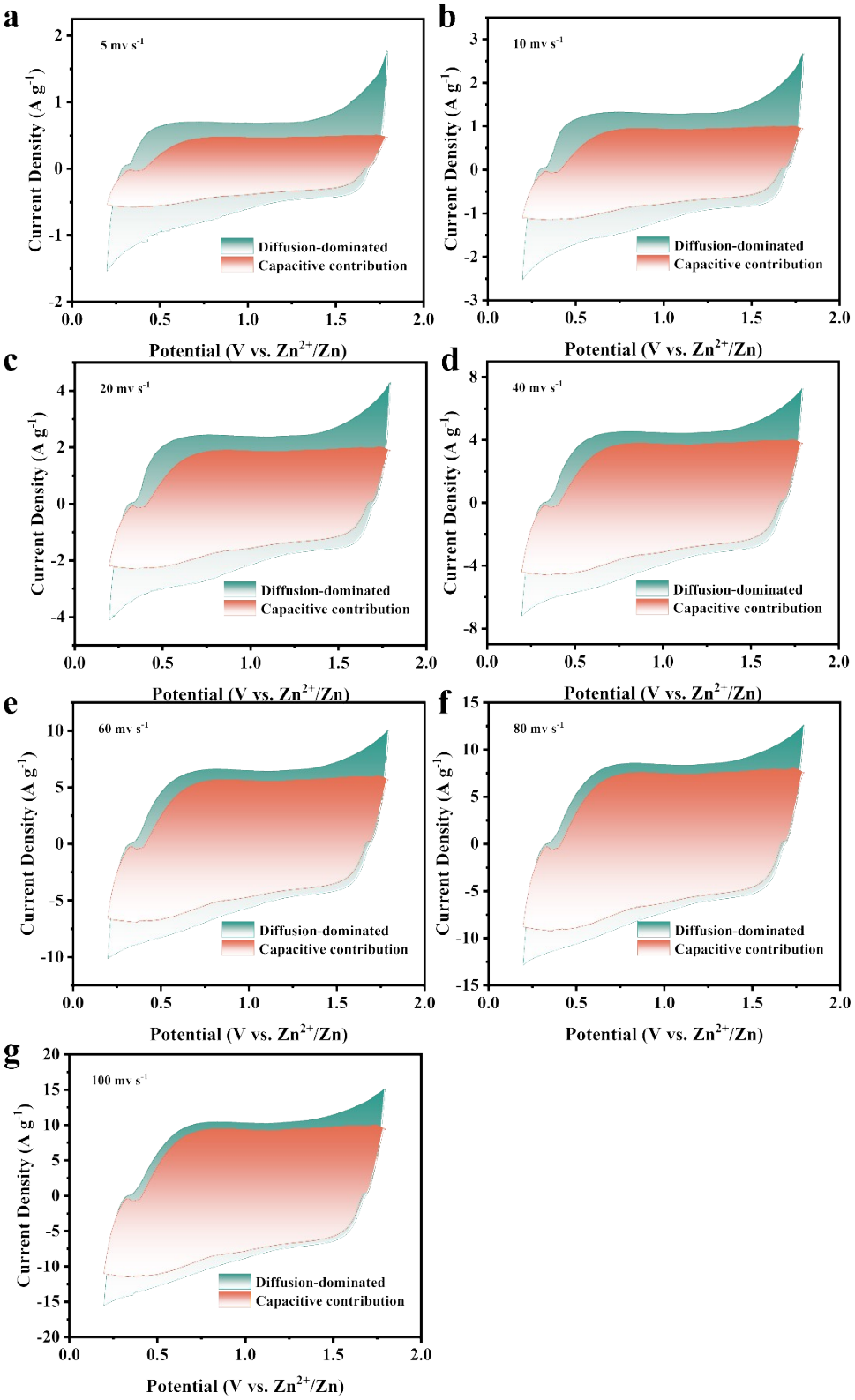


**Fig. S12.** (a - g) Capacitive-controlled and diffusion-dominated contributions of ANC-2 based AZICs from 5 to 100 mV $s^{-1}$

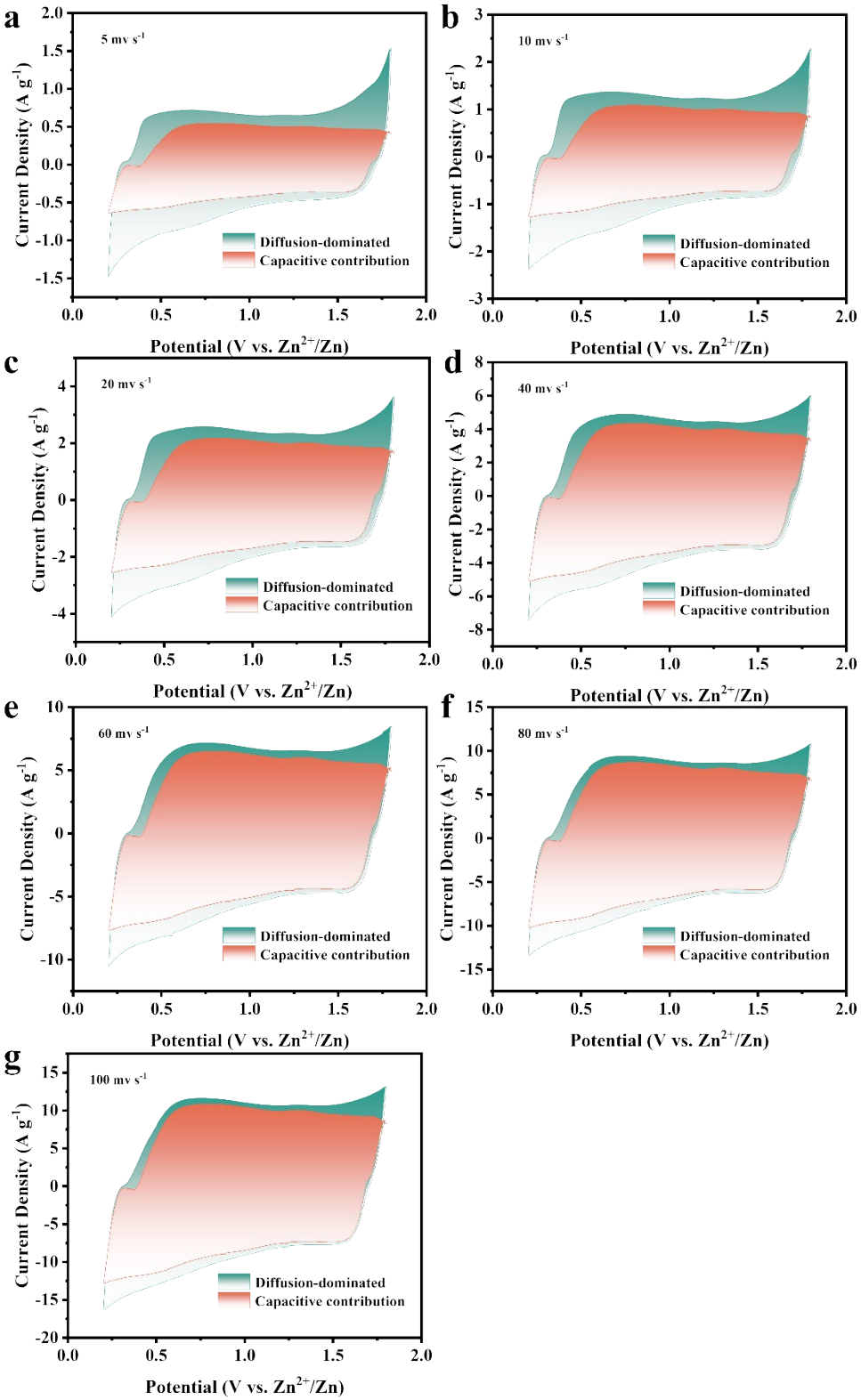


**Fig. S13.** (a - g) Capacitive-controlled and diffusion-dominated contributions of ANC-3 based AZICs from 5 to 100 mV $s^{-1}$

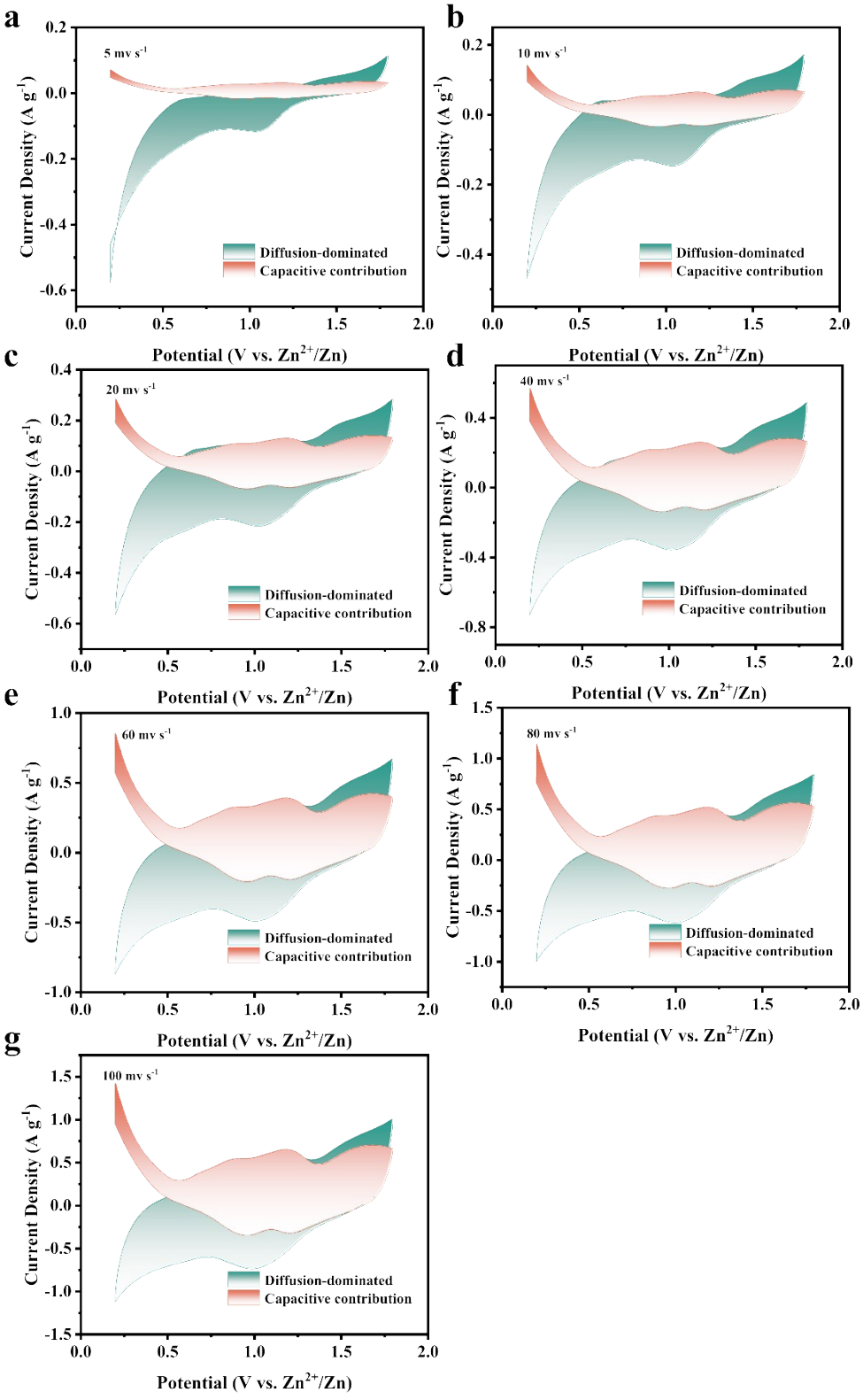


**Fig. S14.** (a - g) Capacitive-controlled and diffusion-dominated contributions of ISC-1 based AZICs from 5 to 100 mV $s^{-1}$

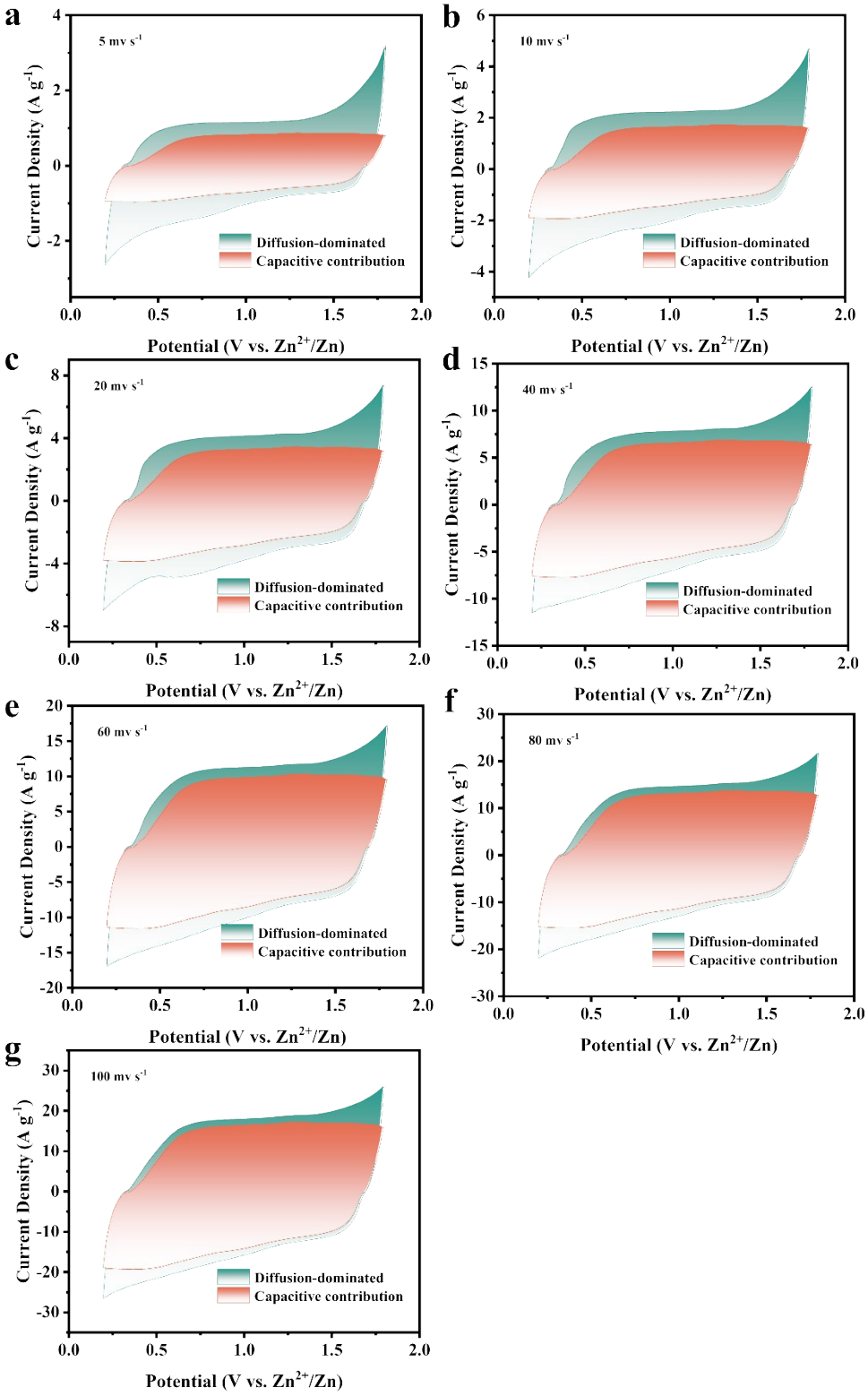


**Fig. S15.** (a - g) Capacitive-controlled and diffusion-dominated contributions of ISC-2 based AZICs from 5 to 100 mV $s^{-1}$

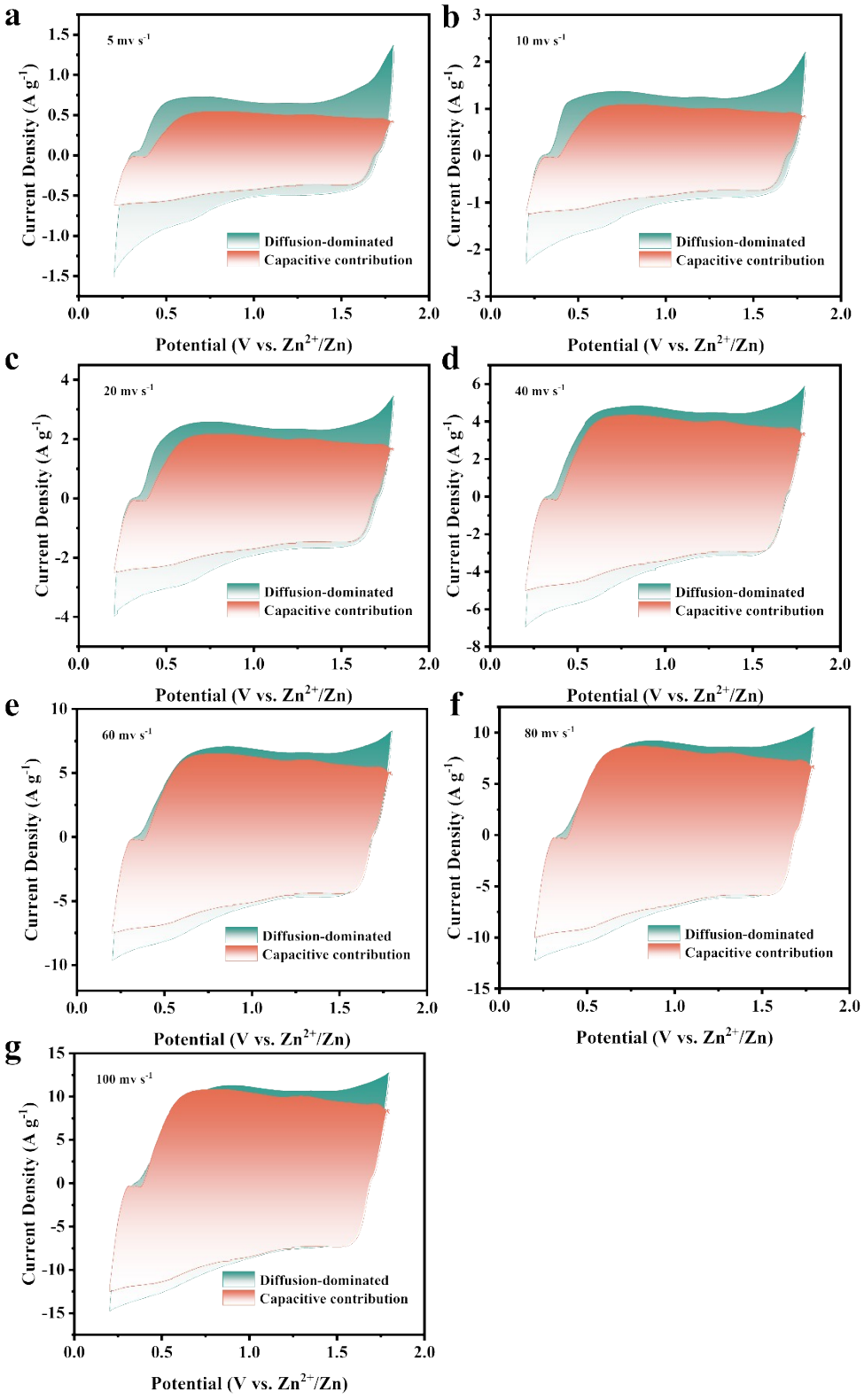


**Fig. S16.** (a - g) Capacitive-controlled and diffusion-dominated contributions of ISC-3 based AZICs from 5 to 100 mV $s^{-1}$

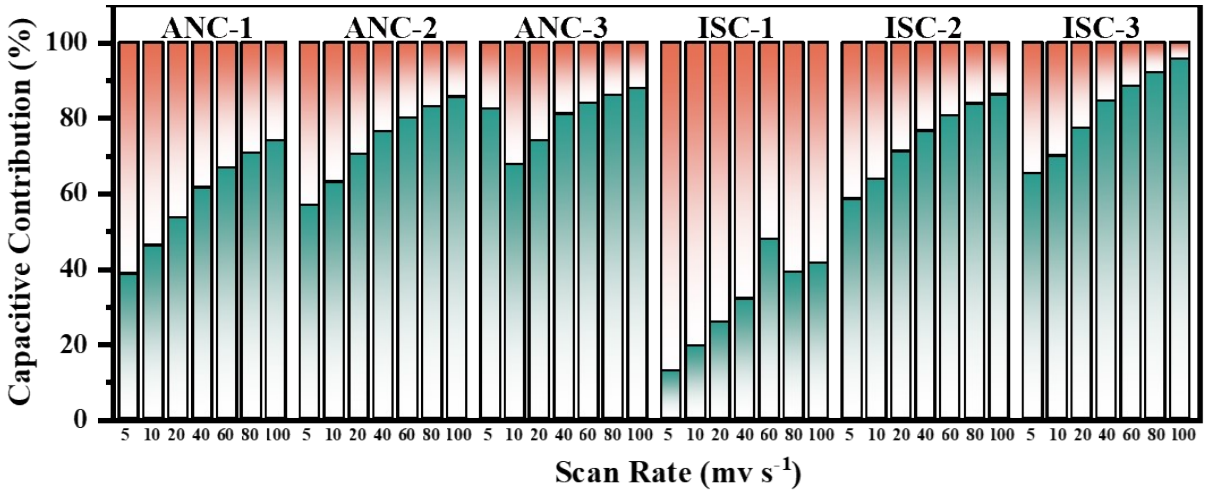


**Fig. S17.** Normalized contribution of capacitance capacity at different scan rates for each sample.

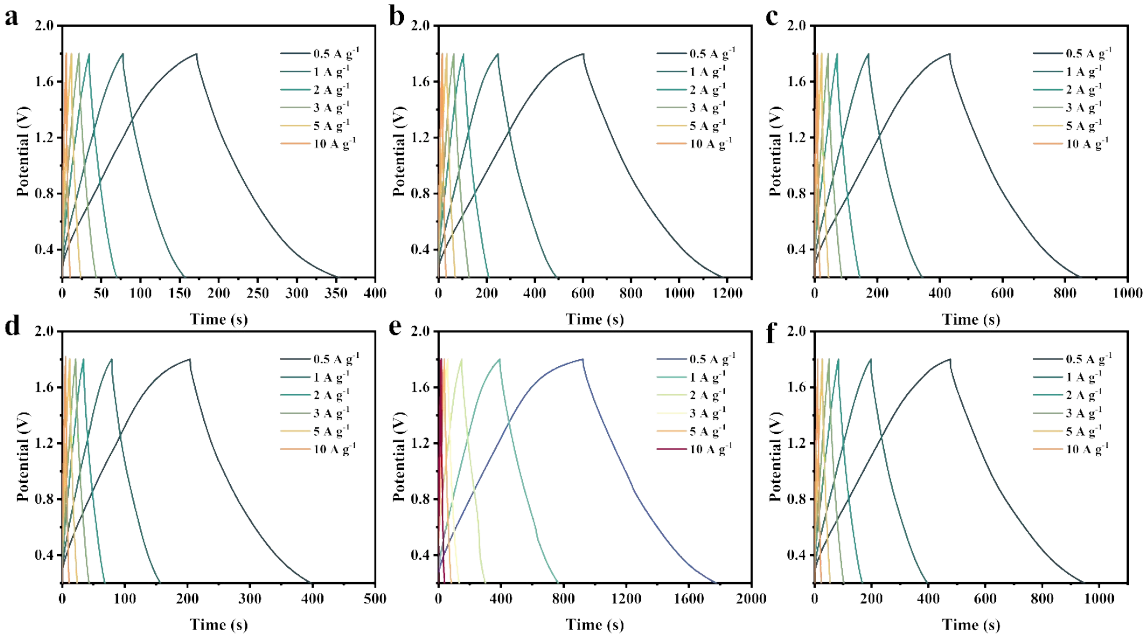


**Fig. S18.** GCD curves of a) ANC-1, b) ANC-2, c) ANC-3, d) ISC-1, e) ISC-2 and f) ISC-3 based AZICs at various current densities from 0.5 to 10 A $g^{-1}$.

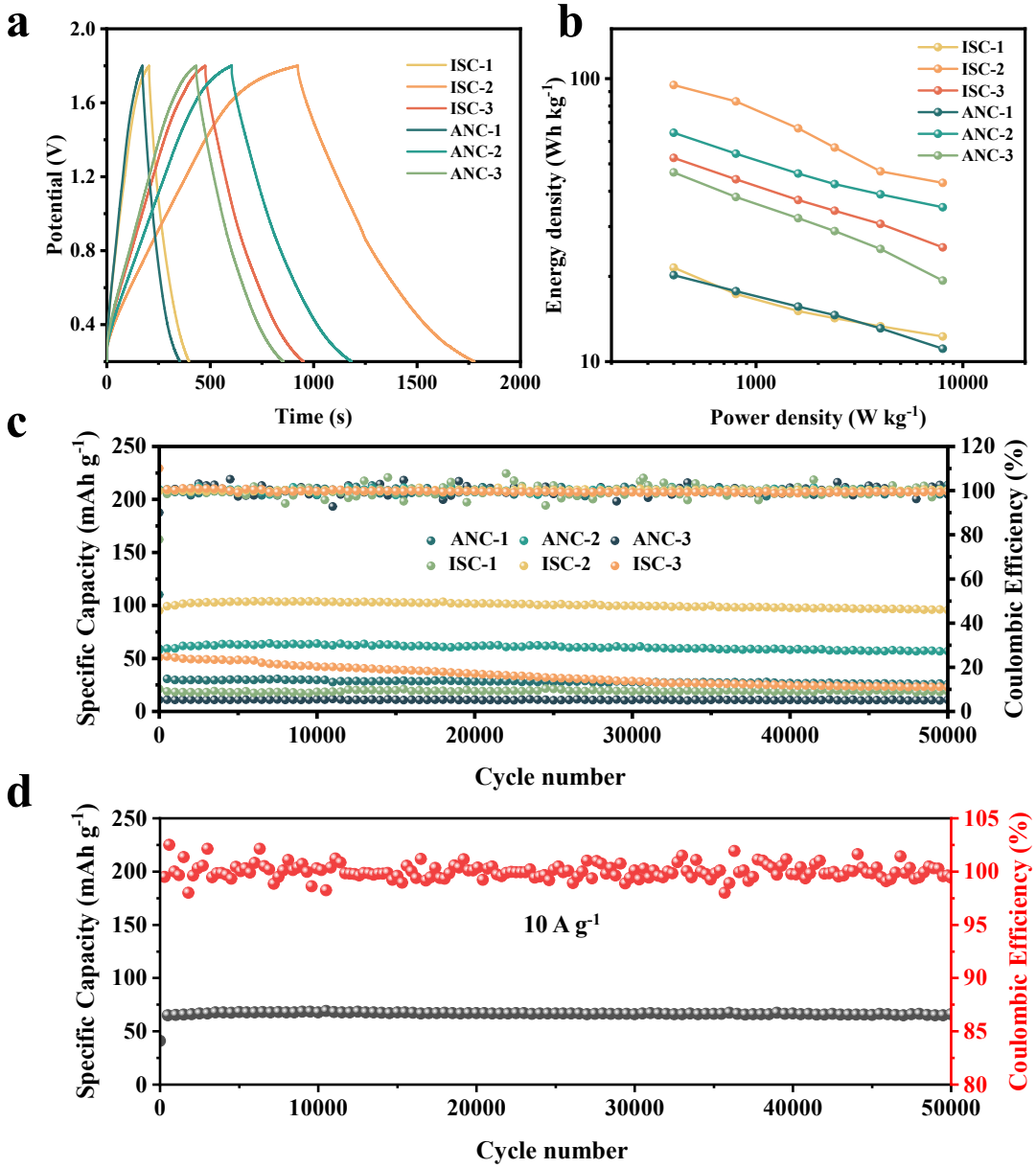


**Fig. S19.** a) GCD curves of ANC-1, ANC-2, ANC-3, ISC-1, ISC-2 and ISC-3 at 0.5 A $g^{-1}$. b) Ragone plot of ANC-1, ANC-2, ANC-3, ISC-1, ISC-2 and ISC-3. c) Cycling stability performances of ANC-1, ANC-2, ANC-3, ISC-1, ISC-2 and ISC-3 at 1 A $g^{-1}$. d) Cycling stability performances of ISC-2 at 10 A $g^{-1}$.

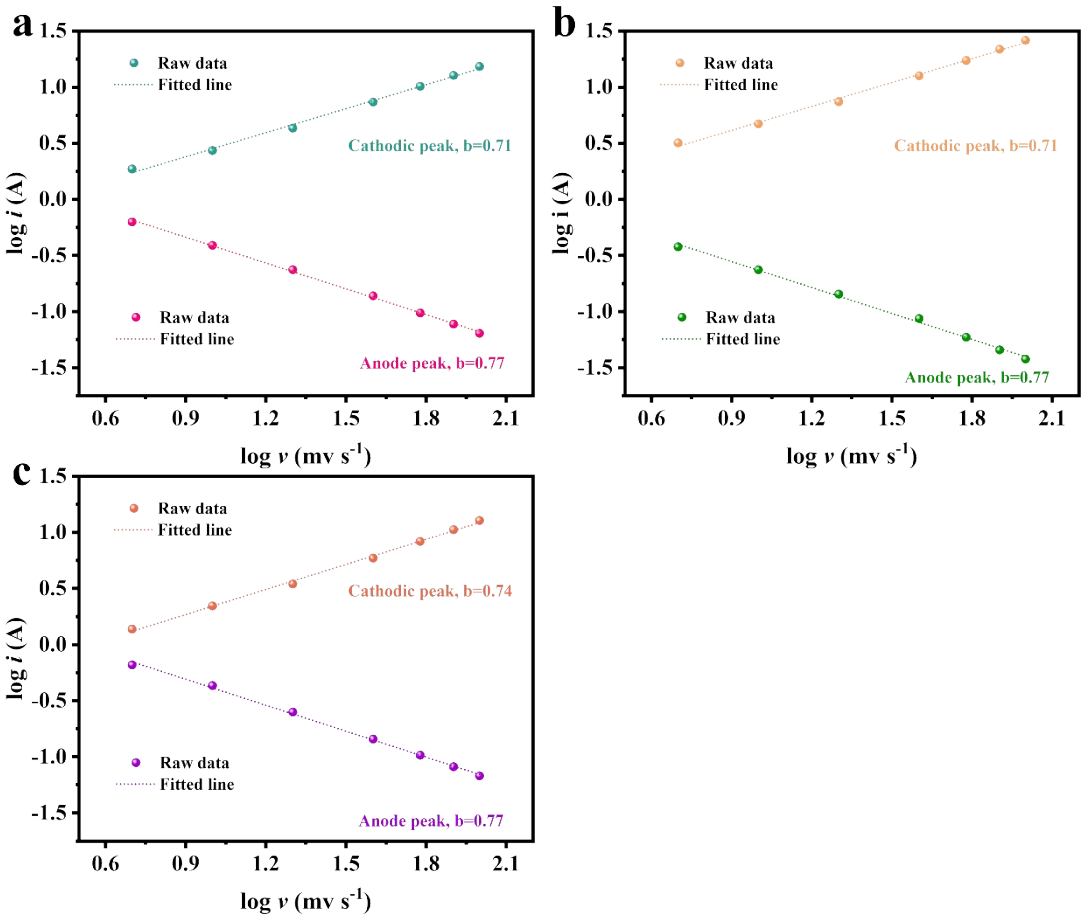


**Fig. S20.** The fitting plot of log (*i*) *vs.* log (*v*) obtained from the peak currents for a) ANC-2, b) ISC-2 and c) ISC-3 cathode.

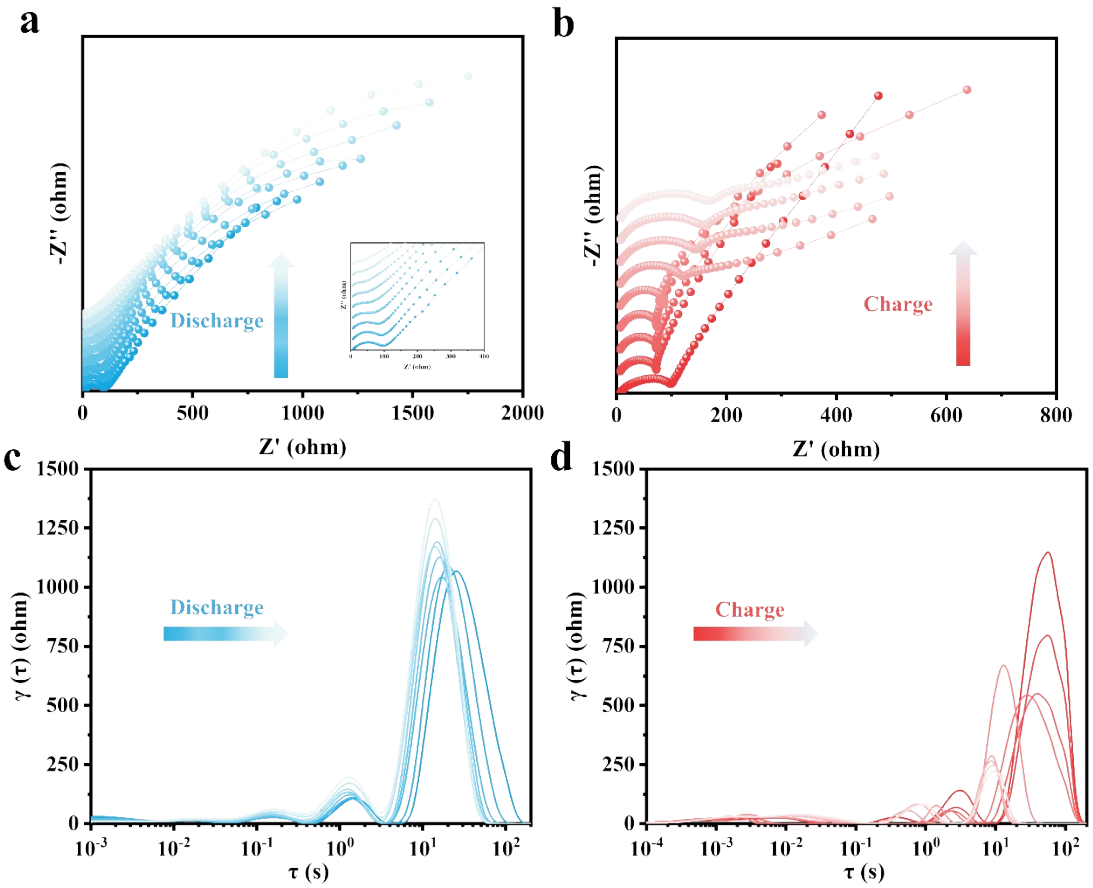


**Fig. S21.** a), b) Nyquist plots of ANC-2 during the discharging/charging process. c), d) DRT calculated from EIS measurements of ANC-2.

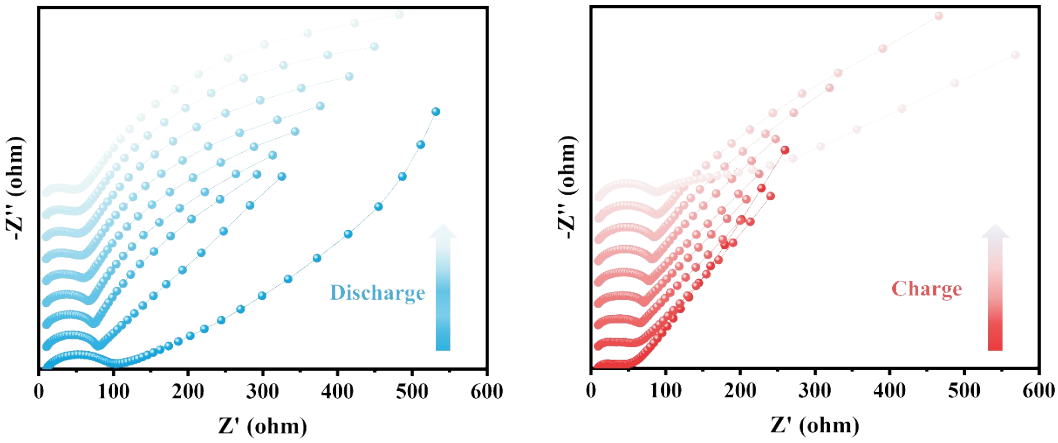


**Fig. S22.** a), b) Nyquist plots of ISC-2 during the discharging/charging process.

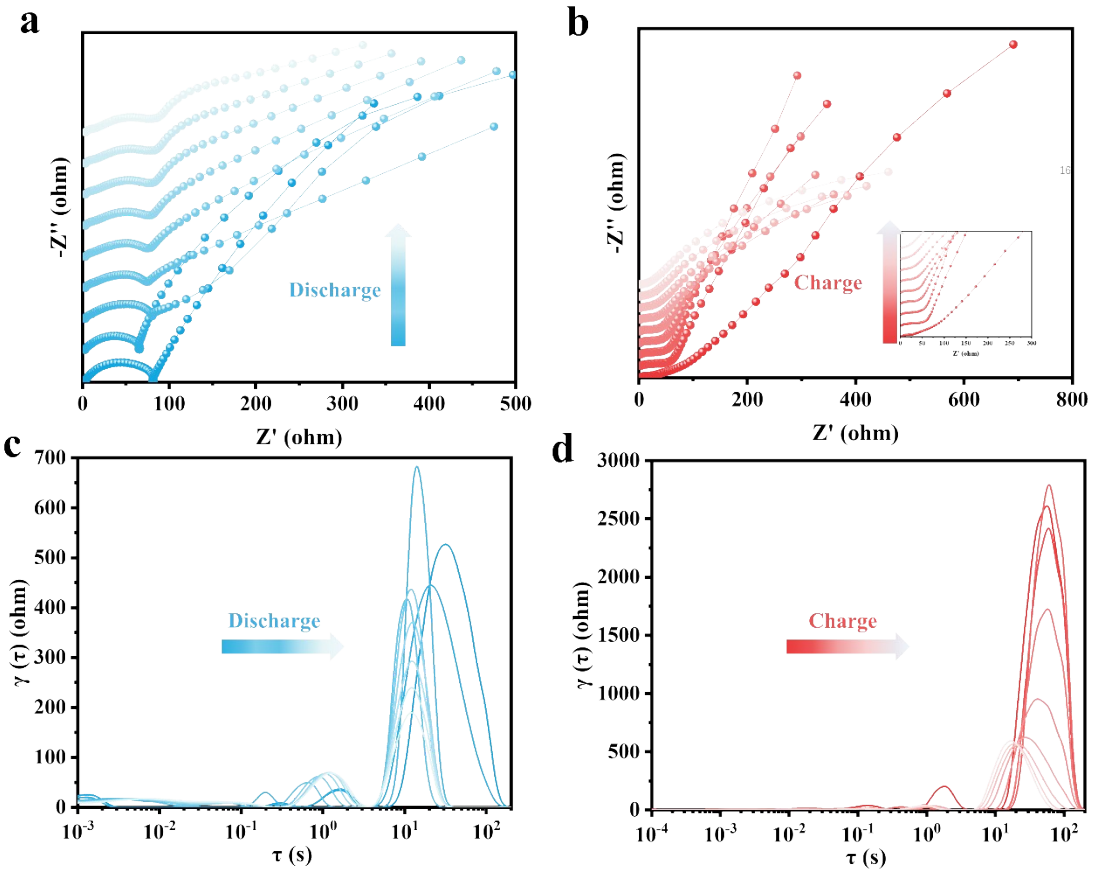


**Fig. S23.** a), b) Nyquist plots of ISC-3 during the discharging/charging process. c), d) DRT calculated from EIS measurements of ISC-3.

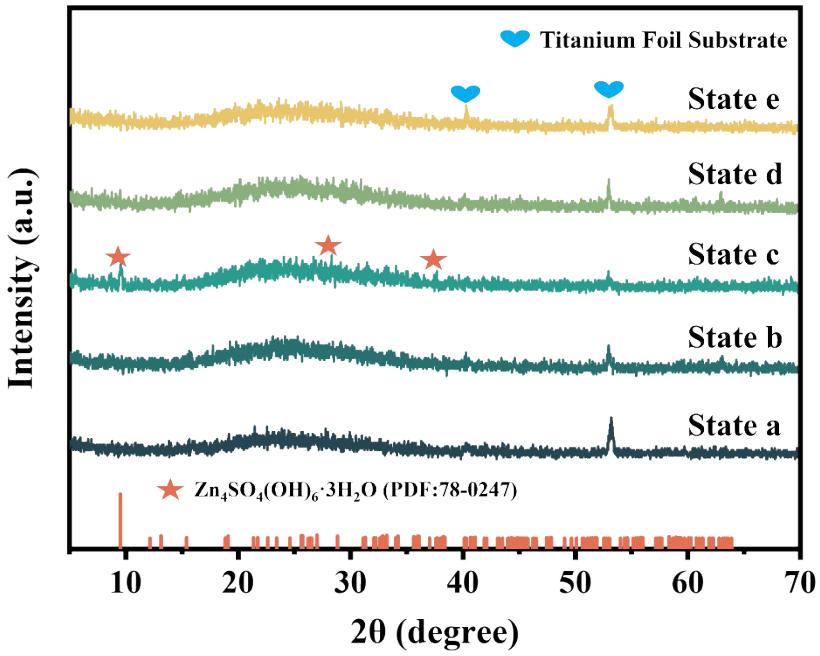


**Fig. S24.** Corresponding ex-situ XRD patterns of ISC-2 at different charge-discharge states.

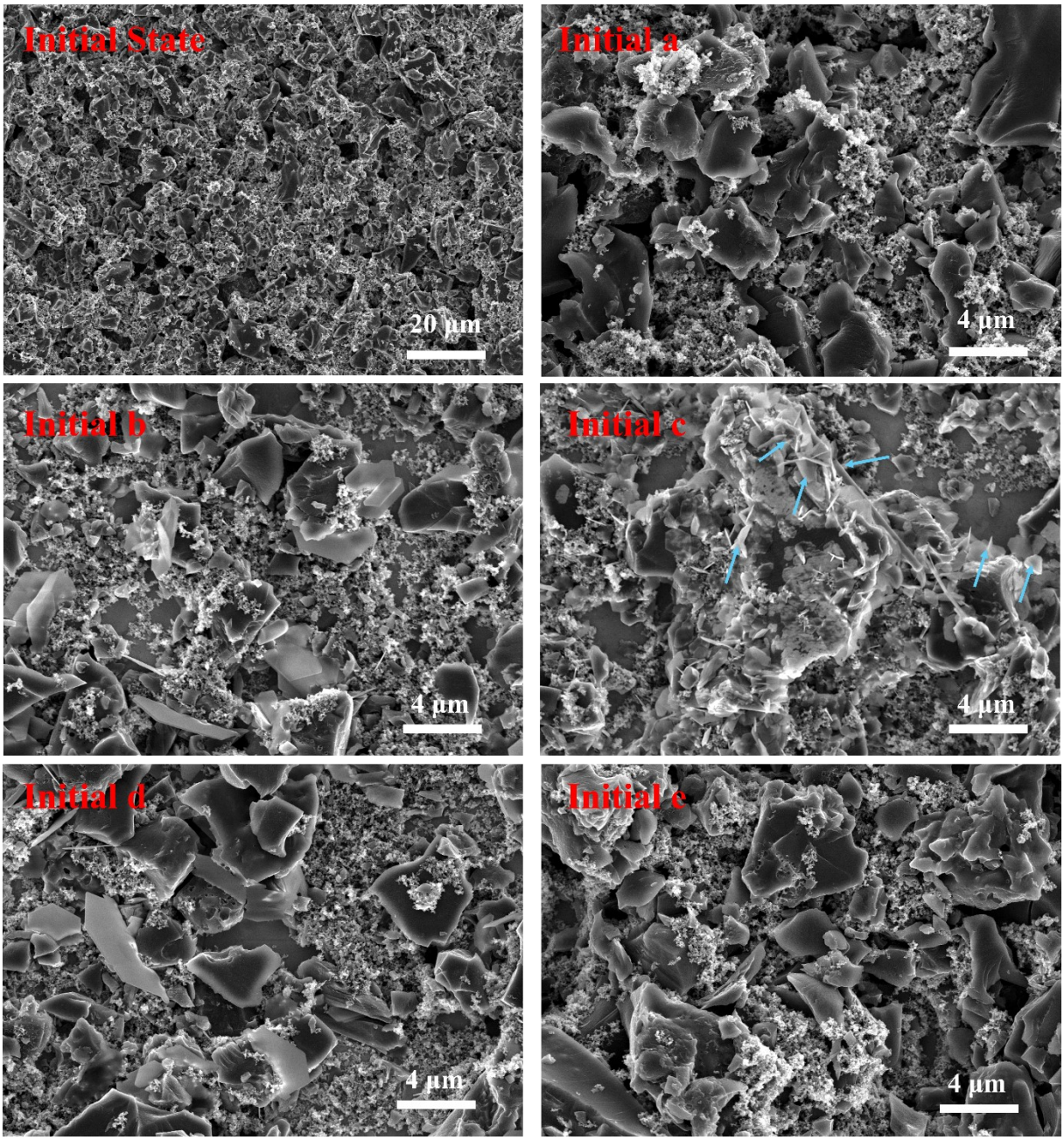


**Fig. S25.** Ex-situ SEM images of ISC-2 cathode at various charge-discharge states.

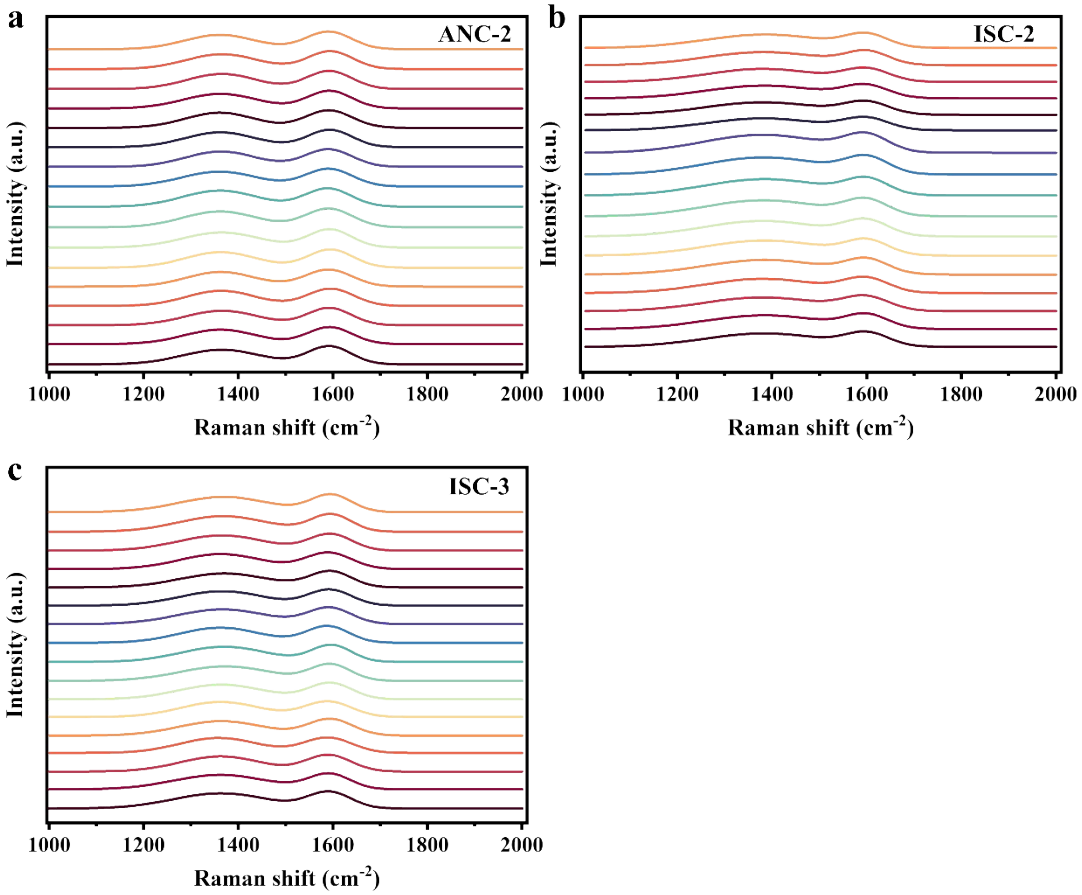


**Fig. S26.** In situ Raman spectra of a) ANC-2, b) ISC-2 and c) ISC-3 during one discharge/charge cycle

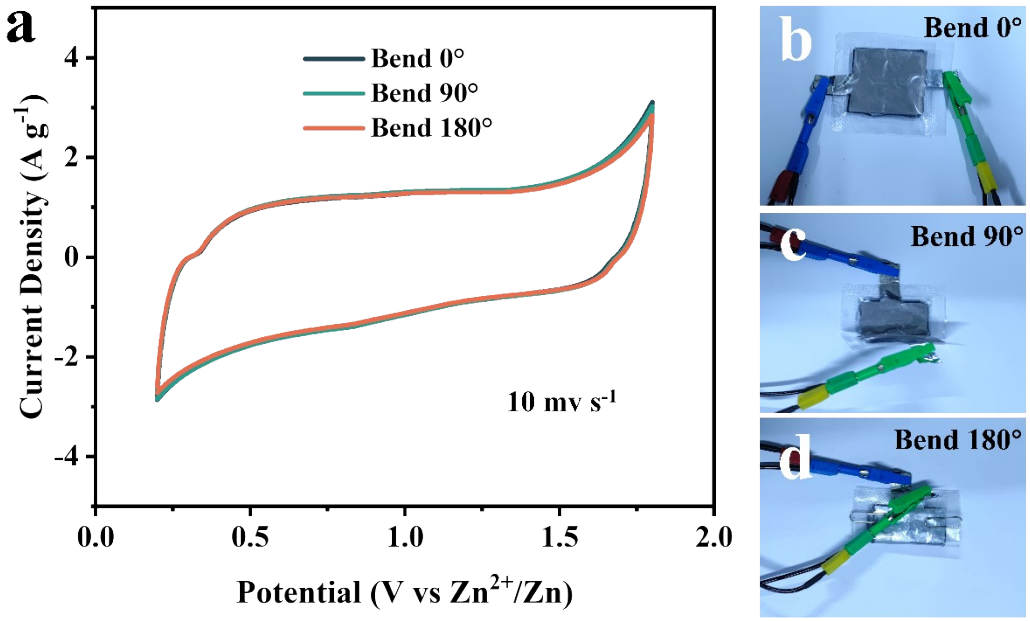


**Fig. S27. CV curves of the device at 0°, 90°, and 180° bending angles.**

**Table S1.** Textural parameters of ISC and ANC samples

| Item | ISC | ANC |
|---|---|---|
| $d_{002}$ (nm) | 0.3489 | 0.3472 |
| $L_c$ (nm) | 1.7924 | 2.2794 |
| $L_a$ (nm) | 3.7057 | 4.7124 |
| n | 5.14 | 6.57 |

$d_{002}$ (nm): Interlayer spacing (aromatic layers)

$L_c$ (nm): Crystallite thickness (Perpendicular to aromatic planes)

$L_a$ (nm): Crystallite diameter (Parallel to aromatic planes)

n: Number of aromatic layers

**Table S2.** Elemental analysis of ISC and ANC samples

| Item | ISC | ANC |
|---|---|---|
| C (wt. %) | 88.60 | 92.80 |
| H (wt. %) | 5.00 | 4.02 |
| S (wt. %) | 0.44 | 0.16 |
| N (wt. %) | 1.83 | 0.02 |
| O (wt. %) | 4.13 | 3.00 |

**Table S3.** Consumed acid volumes (ΔV) of the carbon samples from Boehm titration.

| Samples | ΔNaOH (mL) | $\Delta Na_2CO_3$ (Phenolphthalein) (mL) | $\Delta Na_2CO_3$ (Methyl orange) (mL) | $\Delta NaHCO_3$ (mL) |
|---|---|---|---|---|
| ISC-2 | 1.8 | 1.4 | 2.2 | 1.8 |
| ISC-3 | 0.9 | 0.6 | 0.8 | 1.0 |
| ANC-2 | 0.7 | 1.8 | 1.9 | 0.8 |

**Table S4.** Concentrations of acidic surface functional groups calculated from Boehm titration results.

| Samples | Carboxyl (mmol $g^{-1}$) | β-lactone group (mmol $g^{-1}$) | Phenolic hydroxyl group (mmol $g^{-1}$) | Total acidic group (mmol $g^{-1}$) |
|---|---|---|---|---|
| ISC-2 | 1.8 | 0.8 | -0.4 | 2.6 |
| ISC-3 | 1.0 | 0.2 | 0.3 | 1.5 |
| ANC-2 | 0.8 | 0.1 | -1.1 | 0.9 |

**Table S5.** Pore structure analysis of ISC and ANC samples

| Samples | [a]$S_{BET}$ ($m^2\ g^{-1}$) | [b]$S_{micro}$ ($m^2\ g^{-1}$) | [c]$S_{external}$ ($m^2\ g^{-1}$) | [d]$V_t$ ($cm^3\ g^{-1}$) | [e]$V_{micro}$ ($cm^3\ g^{-1}$) | [f]$V_{external}$ ($cm^3\ g^{-1}$) | [g]$PS_{Average}$ (nm) |
|---|---|---|---|---|---|---|---|
| ISC-1 | 1276 | 1136 | 140 | 0.531 | 0.437 | 0.094 | 3.468 |
| ISC-2 | 1480 | 1447 | 33 | 0.703 | 0.665 | 0.038 | 2.273 |
| ISC-3 | 2886 | 925 | 1961 | 1.444 | 0.388 | 1.055 | 2.471 |
| ANC-1 | 919 | 832 | 87 | 0.379 | 0.324 | 0.055 | 3.080 |
| ANC-2 | 1120 | 1091 | 29 | 0.537 | 0.500 | 0.037 | 2.492 |
| ANC-3 | 2667 | 1300 | 1367 | 1.269 | 0.541 | 0.728 | 2.525 |

[a] BET surface area

[b] t-Plot Micropore Area

[c] $S_{external}=S_{BET}-S_{micro}$

[d] Single-point total pore volume at $P/P_0 = 0.995$.

[e] t-Plot micropore volume

[f] $V_{external} = V_t - V_{micro}$.

[g] Average pore size

**Table S6.** Detailed XPS C 1s peak-fitting parameters for the ISC-2 electrode at different states of charge/discharge.

| Functional Group | Item | State | | | | |
|---|---|---|---|---|---|---|
| | | State a | State b | State c | State d | State e |
| C-C/C=C | Binding energy(eV) | 284.5 | 284.5 | 284.5 | 284.6 | 284.5 |
| | FWHM values | 1.06 | 1.06 | 1.06 | 1.06 | 1.05 |
| | Area ratio (%) | 53.79 | 49.99 | 48.96 | 55.76 | 52.41 |
| C-O | Binding energy(eV) | 285.9 | 286.0 | 286.1 | 286.2 | 285.8 |
| | FWHM values | 1.96 | 1.95 | 1.93 | 1.95 | 1.95 |
| | Area ratio (%) | 24.35 | 27.05 | 25.16 | 23.01 | 30.01 |
| C=O | Binding energy(eV) | 288.4 | 288.5 | 288.4 | 288.6 | 288.3 |
| | FWHM values | 3.18 | 3.15 | 3.16 | 3.18 | 3.15 |
| | Area ratio (%) | 14.38 | 10.11 | 8.06 | 7.46 | 11.82 |
| C-O-Zn | Binding energy(eV) | 290.8 | 290.6 | 290.8 | 290.9 | 290.8 |
| | FWHM values | 1.98 | 1.97 | 1.99 | 1.98 | 1.97 |
| | Area ratio (%) | 7.48 | 12.85 | 17.82 | 13.76 | 5.77 |

**References**


1. B. Zhang, F. Sun, Y. Li, D. Wu, C. Yang, Z. Wang, J. Gao, G. Zhao and S. Sun, *Carbon*, 2024, **219**, 118812.
2. S. Deng, Z. Tie, F. Yue, H. Cao, M. Yao and Z. Niu, *Angewandte Chemie International Edition*, 2022, **134**, e202115877.
3. G. Yang, Q. Zhang, Z. Liu, J. Song, Z. Yin, Y. Zhao, S. Jiang, J. Han, X. Li, H. Yang, S. He and Z. Pei, *Advanced Energy Materials*, 2025, 2501358.
4. X. Li, C. Cai, P. Hu, B. Zhang, P. Wu, H. Fan, Z. Chen, L. Zhou, L. Mai and H. J. Fan, *Advanced Materials*, 2024, **36**, 202400184.
5. Y. Long, X. An, Y. Yang, J. Yang, L. Liu, X. Tong, X. Liu, H. Liu and Y. Ni, *Advanced Functional Materials*, 2025, 2024551.
6. J. Ye, T. Ge, X. Qu, M. M. Mohideen, C. Wang, P. Hu and Y. Liu, *Advanced Functional Materials*, 2025, 202425358.
7. J. Schönherr, J. Buchheim, P. Scholz and P. Adelhelm, *J. Carbon Res.*, 2018, **4**, 21.
8. H. P. Boehm, *Carbon*, 1994, **32**, 759-769.